

Characterizing Evening Solar Terminator Waves in ICON/MIGHTI Neutral Winds

L. Claire Gasque¹, Brian J Harding¹, Thomas J. Immel¹, Yen-Jung Joanne Wu¹, Colin Triplett¹, Sharon L. Vadas², Erich Becker³, and Astrid Maute⁴

¹University of California, Berkeley

²NorthWest Research Associates, Inc.

³Northwest Research Associates

⁴CIRES/ University of Colorado Boulder

November 13, 2023

1 **Evening Solar Terminator Waves in Earth's**
2 **Thermosphere: Neutral Wind Signatures Observed by**
3 **ICON-MIGHTI**

4 **L. Claire Gasque¹, Brian J. Harding¹, Thomas J. Immel¹, Yen-Jung Wu¹,**
5 **Colin C. Triplett¹, Sharon L. Vadas², Erich Becker², Astrid Maute³**

6 ¹Space Sciences Laboratory, University of California, Berkeley, Berkeley, CA

7 ²Northwest Research Associates, Boulder, CO

8 ³High Altitude Observatory, National Center for Atmospheric Research, Boulder, CO

9 **Key Points:**

- 10 • Thermospheric wind measurements above 200 km show a prominent migrating wave
11 associated with the evening solar terminator.
12 • The first observations of solar terminator wave altitude profiles reveal > 200 km
13 vertical wavelengths above 200 km.
14 • Comparison with numerical models suggests a lower atmospheric origin and the
15 potentially significant role of gravity waves.

Corresponding author: L. Claire Gasque, lccgasque@berkeley.edu

Abstract

The moving solar terminator (ST) generates atmospheric disturbances, broadly termed solar terminator waves (STWs). Despite theoretically recurring daily, STWs remain poorly understood, partially due to measurement challenges near the ST. Analyzing Michelson Interferometer for Global High-resolution Thermospheric Imaging (MIGHTI) data from NASA's Ionospheric Connection Explorer (ICON) observatory, we present observations of STW signatures in thermospheric neutral winds, including the first meridional wind signatures. Seasonal analysis reveals STWs are most prominent during solstices, when they intersect the ST about $\sim 20^\circ$ from the equator in the winter hemisphere and have phase fronts inclined at a $\sim 40^\circ$ angle to the ST. We also provide the first observed STW altitude profiles, revealing large vertical wavelengths above 200 km. Comparing these observations to four different models suggests the STWs likely originate directly or indirectly from waves from below 97 km. STWs may play an under-recognized role in the daily variability of the thermosphere-ionosphere system, warranting further study.

Plain Language Summary

Every evening, the sunset removes the primary energy input to the upper atmosphere, causing rapid atmospheric cooling and generating disturbances called solar terminator waves (STWs). Although they theoretically occur every night, STWs remain poorly understood, partially because the rapidly changing atmospheric conditions near sunset make measurements challenging. This study examines neutral wind measurements from the Michelson Interferometer for Global High-resolution Thermospheric Imaging (MIGHTI) on board NASA's Ionospheric Connection Explorer (ICON) observatory to uncover signatures of STWs. We report the north-south wind signatures of STWs and their altitude profile from 200-300 km, both of which have never been previously reported. We show that STWs are some of the largest amplitude dynamical features above 200 km near solstices, but are much weaker near equinoxes. By comparing our observations with the outputs of four different models, we find that STWs are likely generated directly or indirectly (from wave propagation) below 97 km. Future work is necessary to better understand how STWs are generated, how they vary on a daily basis, and the extent of their impacts on Earth's upper atmosphere.

1 Introduction: Solar Terminator Waves in the Terrestrial Thermosphere

Every night, the evening solar terminator (ST) sweeps across Earth, dividing daylight from shadow and interrupting the solar radiation which plays a key role in atmospheric heating and ionospheric plasma production. This generates abrupt gradients in atmospheric temperature and pressure, which can launch disturbances in the mesosphere and thermosphere (Somsikov, 2011). Broadly termed solar terminator waves (STWs), these disturbances form near and propagate with the advancing ST (Miyoshi et al., 2009). Although they theoretically recur every night, STWs' morphology and occurrence patterns remain poorly characterized, and their specific generation mechanisms are still debated.

STW generation theory first emerged when, inspired by Chimonas and Hines (1970)'s anticipation of gravity waves excited by time-variable heating during solar eclipses, Beer (1973) proposed a similar effect from the daily motion of the ST. Subsequent research delved deeper into the theoretical underpinnings of STWs, generally confirming that the moving ST can generate gravity waves, but the scarcity of observations hampered further advancement of this work (Beer, 1978; Cot & Teitelbaum, 1980; Somsikov, 1987; Somsikov & Ganguly, 1995).

64 Only three studies have reported observations of STWs in the thermosphere. Using
 65 the CHAMP satellite’s tri-axial accelerometer, Forbes et al. (2008) identified an STW
 66 in thermospheric neutral densities. These had a ~ 3000 km horizontal wavelength, had
 67 phase fronts inclined $\sim 30^\circ$ with respect to the ST, and were more pronounced during
 68 solstices than equinoxes. Subsequently, H. Liu et al. (2009) confirmed the density STW
 69 and also detected an STW in CHAMP’s thermospheric cross-track (i.e. mainly zonal)
 70 winds. The zonal wind STW had comparable wavelength and inclination to the ST as
 71 the density STW, with zonal wind magnitudes ranging from 5-15 m/s, constituting 5-
 72 20% of the mean zonal wind velocity at those local times. Both studies concluded that
 73 the STW was more prominent at dusk than at dawn, with most wave structures appear-
 74 ing on the nightside, only extending into the sunlit region around solstices. These results
 75 correlated well with General Circulation Model (GCM) simulations conducted by Forbes
 76 et al. (2008) and Miyoshi et al. (2009). In a third study, Bespalova et al. (2016) exam-
 77 ined in-situ neutral density perturbations detected by the Atmospheric Explorer-E satel-
 78 lite, finding density perturbations with amplitudes of 2-4% associated with the ST pas-
 79 sage.

80 Recent modeling by Chou et al. (2022) and Vadas et al. (2023) suggests that STWs
 81 in neutral winds could have a more significant impact on equatorial thermospheric dy-
 82 namics than previously considered. Using a Specified Dynamics Whole Atmosphere Com-
 83 munity Climate Model with thermosphere-ionosphere eXtension (SD-WACCM-X) simu-
 84 lation from October 2020, Chou et al. (2022) identified a large-amplitude evening STW
 85 with phase fronts aligned from northwest to southeast, the same orientation as winter
 86 solstice STWs observed with CHAMP (Forbes et al., 2008; H. Liu et al., 2009). Chou
 87 et al. (2022) proposed that evening STWs play an underrecognized role in driving equa-
 88 torial electrodynamic phenomena such as equatorial plasma bubbles (EPBs). Addition-
 89 ally, Vadas et al. (2023) identified STWs with horizontal wind magnitudes of 50-100 m/s
 90 in a High Altitude Mechanistic general Circulation Model (HIAMCM) simulation of 15
 91 January 2022. Although their primary focus was simulating the primary and secondary
 92 gravity waves triggered by the Hunga Tonga-Hunga Ha’apai volcanic eruption, the STW
 93 was surprisingly prominent in the simulation results and interacted non-linearly with the
 94 eruption-induced gravity waves. While both studies report STWs with significant neu-
 95 tral wind amplitudes and emphasize their potential influence on thermospheric and iono-
 96 spheric dynamics, these conclusions remain to be confirmed with observational evidence.

97 This study presents the first remotely-sensed measurements of evening STWs in
 98 thermospheric neutral winds, including the first STW meridional wind observations. By
 99 analyzing ~ 1.5 years of data from NASA’s Ionospheric Connection Explorer (ICON)
 100 satellite, we investigate seasonal variation in STWs, and compare these findings to sim-
 101 ulations from several models. We also present the first observed altitude profiles of ther-
 102 mospheric evening STWs, comparing our observations with HIAMCM simulation results.
 103 This work confirms that STWs are prominent features in the terrestrial thermosphere,
 104 suggesting the necessity of future modeling and observational studies which will further
 105 enhance our understanding of STW drivers and effects.

106 **2 Methods: Observations and Modeling**

107 **2.1 ICON/MIGHTI Neutral Wind Observations**

108 In this study, we examine evening STW signatures in neutral wind measurements
 109 from ICON’s Michelson Interferometer for Global High-Resolution Thermospheric Imag-
 110 ing (MIGHTI). ICON follows a nearly circular orbit with 27° inclination at ~ 600 km and
 111 achieves complete local time coverage across sampled latitudes every ~ 48 days (Immel
 112 et al., 2018). Further details about ICON’s design and objectives can be found in Immel
 113 et al. (2018), and the significant findings from its prime mission period are outlined in
 114 Immel et al. (2023).

MIGHTI measures Doppler shifts in oxygen airglow emissions to determine horizontal neutral wind profiles between -12° and $+42^\circ$ latitude (Englert et al., 2017). Unlike CHAMP, which made in situ measurements, ICON remotely measures neutral wind altitudinal profiles, enabling observations of the vertical structure of STWs. MIGHTI captures daytime wind profiles every 30 seconds between 90 and 300 km. Nighttime winds are sampled every 60 seconds at the same altitudes, except for a gap spanning ~ 109 to 210 km where the airglow brightness is insufficient to take reliable measurements (Harlander et al., 2017; Harding et al., 2021).

Here, we use MIGHTI Level 2.2 Version 5 data, which provides meridional and zonal neutral wind measurements. Near the ST, there is a brief data gap when MIGHTI switches from day to night mode (Englert et al., 2023). Additionally, the MIGHTI wind retrieval algorithm assumes that the atmosphere is spherically symmetric, but this assumption is violated by the rapidly changing conditions near the ST (Harding et al., 2017). While the resulting asymmetry-associated errors can surpass 10 m/s near 150 km, above 200 km these errors are expected to be less than 1 m/s and therefore should not affect our analysis (Wu et al., 2020). Furthermore, Version 5 incorporates three updates important for improving the wind data quality near the ST: an independent, higher accuracy zero-wind calibration, an updated thermal drift correction, and a correction for the “anomalous low-signal phase shift” (Englert et al., 2023). Additional details about the MIGHTI instrument design and data processing can be found in Englert et al. (2017), Harding et al. (2017), and Harlander et al. (2017), while the updated Version 5 processing is detailed in Englert et al. (2023).

Due to the significant variations in STW morphology between seasons (Forbes et al., 2008; H. Liu et al., 2009), we divide the data into three seasons for analysis: northern hemisphere (NH) winter, combined equinox, and NH summer. Spring and autumn are combined as they exhibit minimal differences in our analysis. For each season, we include data captured in the period from 45 days before to 45 days after the corresponding solstice or equinox, encompassing 90 days total or nearly 2 full precession cycles. While MIGHTI data is available almost continuously from December 2019 to November 2022, the SD-WACCM-X simulations used for comparison (see Section 2.2) only extend until March 27, 2021. Consequently, we limit our analysis to this period (Dec 2019 - March 2021), covering 2 NH winters, nearly 3 equinoxes, and 1 NH summer. Extending our analysis to the end of the mission does not alter our observational conclusions. With the exception of some moderate solar activity in November 2020, all of the data surveyed here is for solar quiet ($F_{10.7} < 80$) conditions (Wu et al., 2023). This period also encompasses a small geomagnetic storm, described in McGinness et al. (2023).

We bin the meridional and zonal winds for each season into 30-minute solar local time (SLT) intervals and 1° latitude bins, taking the median value in each bin. By averaging over all longitudes, we selectively retain features traveling with Earth’s rotation, filtering out non-migrating components (Miyoshi et al., 2009). MIGHTI’s horizontal resolution is affected by its integration time, horizontal field of view, line-of-sight averaging, and the spacecraft velocity, as detailed in Harding et al. (2021)’s Appendix. These combined effects can lead to a blur of up to 1200 km at lower altitudes during daytime, but resolution improves to ~ 400 km at higher altitudes, which are our focus here. Our 30-minute SLT bins are equivalent to roughly 850 km resolution. Given an expected evening STW scale size of ~ 3000 km (Forbes et al., 2008), the resolution is sufficient for capturing these features. Although data sampled within ~ 500 km of the ST carries a ‘caution’ label in MIGHTI’s data quality flags, we nonetheless include this data in our analysis. Despite binning and averaging the data, some artifacts near the ST persist, especially in NH summer where we incorporate only a single season of data. However, since any data artifacts have a much smaller scale than the evening STWs, and are oriented exactly parallel to the ST, they are not expected to affect our conclusions.

167 In the cases where we find the largest evening STW amplitudes, we further char-
 168 acterize the STW’s morphology. First, we remove diurnal variations as a function of SLT
 169 at each latitude by fitting and subtracting a 24-hour period sinusoid (representing the
 170 diurnal tide). Then, we fit a Gaussian near the evening ST at each latitude, determin-
 171 ing the amplitude and estimating the scale size as the 2-standard deviation width. The
 172 reported amplitudes and scale sizes in Section 3 represent averages across all latitudes
 173 observed by MIGHTI. By fitting a line to the STW as a function of latitude and SLT
 174 and intersecting it with the ST’s position, computed using the method described in Colonna
 175 and Tramutoli (2021), we determine the latitude of intersection and the STW’s angle
 176 relative to the ST.

177 2.2 Simulations

178 To determine whether current global models capture the physics necessary to re-
 179 produce STW signatures observed by MIGHTI, we compare the observations to simu-
 180 lations from three different models: the Thermosphere-Ionosphere-Electrodynamics Gen-
 181 eral Circulation Model for the Ionospheric Connection Explorer (TIEGCM-ICON) (Maute,
 182 2017), SD-WACCM-X 2.0 (H.-L. Liu et al., 2018), and the HIAMCM (Becker & Vadas,
 183 2020; Becker, Vadas, et al., 2022; Becker, Goncharenko, et al., 2022).

184 The TIEGCM describes thermospheric and ionospheric dynamics, energetics, and
 185 chemistry, coupled with ionospheric electrodynamics (Richmond, 1995; Qian et al., 2014).
 186 In this study, we used TIEGCM-ICON, ICON’s Level 4 data product (Maute, 2017; Maute
 187 et al., 2023), which includes two runs of the TIEGCM: a simulation which incorporates
 188 data-driven 42-day averages of diurnal and semidiurnal tidal forcing at the 97 km lower
 189 boundary via the Hough Mode Extension (HME) from MIGHTI horizontal winds and
 190 temperatures (Forbes et al., 2017; Cullens et al., 2020), and one without such a tidal spec-
 191 ification. The background at the lower boundary is obtained from global averages of hor-
 192 izontal winds (Drob et al., 2008) and neutral temperatures and densities (Picone et al.,
 193 2002). The model resolution is 2.5° by 2.5° in geographic latitude and longitude and the
 194 numerical damping suppresses features with wavelengths below ~ 2500 km. This model
 195 does not include gravity waves generated below its lower boundary, although it implic-
 196 itly incorporates some effects of turbulent mixing due to gravity wave breaking by spec-
 197 ifying the eddy diffusivity at the lower boundary (Qian et al., 2014). This method does
 198 not, however, account for the spatial distribution of lower/middle atmosphere gravity
 199 wave sources.

200 Unlike the TIEGCM, SD-WACCM-X 2.0 includes lower atmospheric dynamics to
 201 capture large-scale day-to-day variations (H.-L. Liu et al., 2018). We use the run per-
 202 formed by England et al. (2022), which is nudged to GEOS-5. The detailed lower atmo-
 203 spheric physics, including tropospheric weather, deep convection, and ozone variability,
 204 are described by Marsh et al. (2013) and Neale et al. (2013). The SD-WACCM-X sim-
 205 ulations we use have 0.9° by 1.25° resolution in latitude and longitude, respectively, ca-
 206 pable of resolving features with wavelengths larger than ~ 500 km. To account for small-
 207 scale gravity wave momentum deposition, SD-WACCM-X includes a gravity wave parametriza-
 208 tion, detailed by Richter et al. (2010) and Garcia et al. (2017), which identifies gravity
 209 wave sources (e.g. convection, fronts, orographic features) and incorporates resulting wave
 210 dissipation effects into the simulations.

211 The TIEGCM (with and without HMEs) and SD-WACCM-X simulations in this
 212 analysis cover the period from ICON mission’s start until spring 2021. We sampled model
 213 outputs at the same times and locations as MIGHTI data, and processed this “synthetic
 214 data” in the same manner as the MIGHTI data (described in Section 2.1).

215 We also compare NH winter STW results from the HIAMCM, a high-resolution global
 216 whole-atmosphere model for neutral dynamics. The HIAMCM’s horizontal grid spac-
 217 ing is ~ 52 km ($\sim 0.45^\circ$), enabling it to effectively resolve waves with horizontal scales

218 above ~ 200 km, smaller than the TIEGCM and SD-WACCM-X simulations examined
 219 here (Becker, Vadas, et al., 2022). This model also incorporates lower atmospheric pro-
 220 cesses, detailed in Becker and Vadas (2020), with large scales nudged to Modern-Era Ret-
 221 rospective analysis for Research and Applications, Version 2 (MERRA-2) reanalysis up
 222 to ~ 70 km. Unlike the other models, the HIAMCM explicitly resolves gravity waves,
 223 including both primary gravity waves and the secondary gravity waves which arise from
 224 dissipation of the primaries (Becker & Vadas, 2020; Becker, Goncharenko, et al., 2022).
 225 Resolved gravity wave packets that become dynamically unstable are damped by physics-
 226 based subgrid-scale turbulent diffusion, simulating wave-mean flow interactions caused
 227 by wave instability and subsequent dissipation (Lindzen, 1981). The HIAMCM neglects
 228 non-local momentum and energy transfer caused by non-resolved gravity waves.

229 This study uses the HIAMCM ‘background’ run from 15 January 2022, which ex-
 230 cludes the effects of the Tonga volcano eruption on that day and the geomagnetic storm
 231 on the day prior (Vadas et al., 2023). To facilitate comparisons, we bin and average the
 232 data from every time step of the simulation as functions of the same latitude and SLT
 233 bins used for MIGHTI and extract the STW features in the same manner.

234 3 Results

235 Figure 1(a) presents NH winter MIGHTI meridional winds at ~ 283 km, binned and
 236 averaged as a function of latitude and SLT. This altitude was chosen to minimize terminator-
 237 related data artifacts. Gray shading marks nighttime regions (for which the sun is be-
 238 low the horizon) at this altitude. Note that, although none of the tides have been removed
 239 in Figure 1(a), the evening STW is a prominent feature in the meridional winds, appear-
 240 ing as a northward wind enhancement near the evening ST (the transition between il-
 241 lumination and shadow near 20 SLT). At most MIGHTI-sampled latitudes, the STW-
 242 related enhancement corresponds to the largest total meridional wind amplitude with
 243 respect to SLT, suggesting its potentially significant role in thermospheric and ionospheric
 244 dynamics, including field-aligned ion drag and interhemispheric transport (Heelis et al.,
 245 2022).

246 The second row of Figure 1 shows the tidal decomposition of Figure 1(a) into its
 247 diurnal (Figure 1(b)), semidiurnal (Figure 1(c)), and terdiurnal (Figure 1(d)) compo-
 248 nents. These components were obtained by fitting sinusoids with 24-hour, 12-hour, and
 249 8-hour periods, respectively, as a function of SLT at each latitude. The amplitude of the
 250 colorbar is reduced for each successive tidal component, reflecting the diminishing power
 251 in each subsequent component. The final row (Figures 1(e), 1(f), and 1(g)) displays the
 252 residuals in the data after removing each successive tidal component.

253 Figure 2 shows the corresponding tidal decomposition of the observed zonal winds.
 254 In this case, the diurnal tide is more dominant than in the meridional winds, with the
 255 binned wind measurements in Figure 2(a) showing a clear pattern of westward winds dur-
 256 ing the day and eastward winds at night. However, with the removal of the diurnal tidal
 257 component (Figure 2(e)), an enhanced eastward wind feature emerges which has a sim-
 258 ilar amplitude and proximity to the evening ST as the northward meridional wind en-
 259 hancement.

260 With the successive removal of the migrating diurnal, semidiurnal, and terdiurnal
 261 tidal components, the STW amplitude is reduced, although a distinct signature persists.
 262 This suggests the STW has power in multiple tidal components and is not attributable
 263 to any individual tide. Therefore, in the subsequent analysis, we characterize the STW
 264 after removing only the migrating diurnal tidal component.

265 Figure 3 displays binned MIGHTI meridional and zonal winds at ~ 283 km for NH
 266 winter, combined equinox, and NH summer after removing the migrating diurnal tide.
 267 Black dotted lines identify the STW feature in the solstice cases. The NH winter STW

MIGHTI NH Winter Meridional Wind (~283 km): Migrating Tide Removal

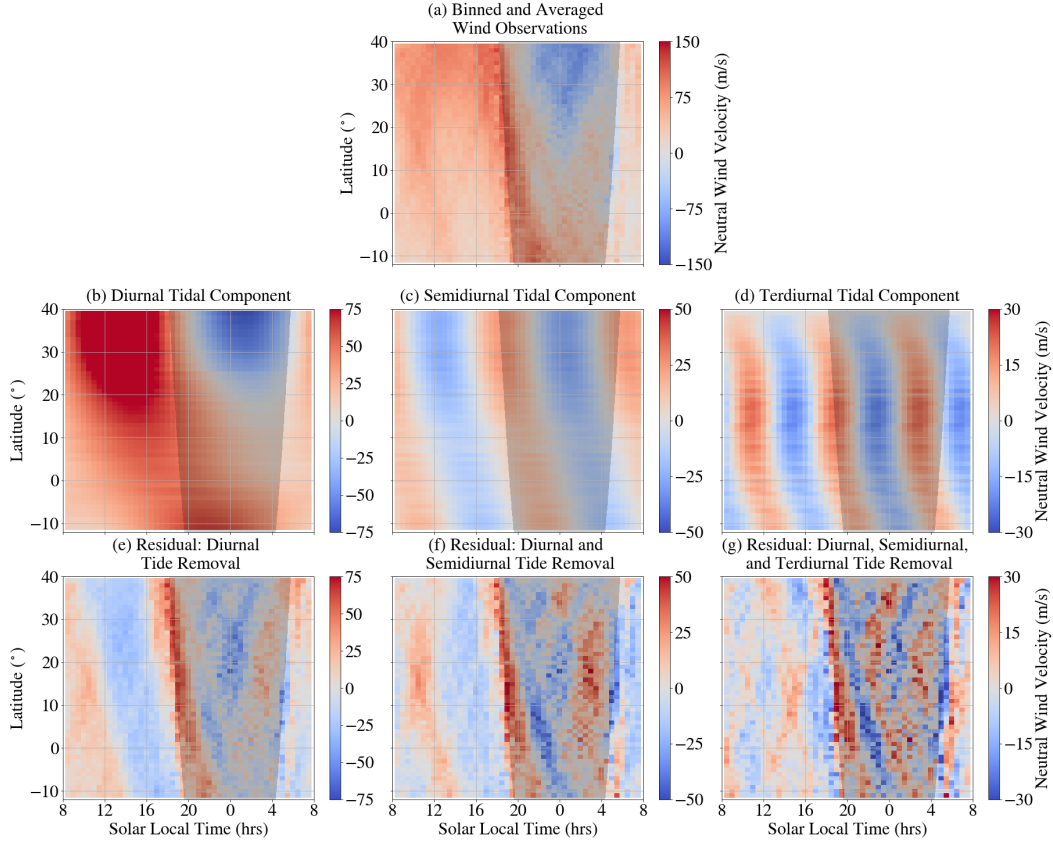


Figure 1. Meridional winds during NH winter as observed by MIGHTI, presented as a function of latitude and SLT. In the first row, (a) shows the binned and averaged data prior to the removal of tidal components. The second row displays the fits for the (b) diurnal, (c) semidiurnal, and (d) terdiurnal tidal components. The final row shows the data residuals after successively removing the (e) diurnal, (f) semidirunal, and (g) terdiurnal tides. Note that the colorbar amplitude varies between subfigures.

268 is characterized by ~ 50 m/s northward winds (Figure 3(a)) and ~ 50 m/s eastward winds
 269 on the nightside, although the zonal wind component diminishes on the dayside (Fig-
 270 ure 3(b)). In both meridional and zonal wind components, it has a ~ 2900 km scale size,
 271 intersecting the ST between $\sim 15^\circ$ to 20° latitude (~ 18.8 SLT) with a $\sim 31^\circ$ phase front
 272 inclination compared to the ST.

273 For the NH summer case, MIGHTI's latitude sampling does not reach father south
 274 than -12° , where we might expect the NH summer STW to intersect the evening ST.
 275 However, we observe a ~ 40 m/s southward wind enhancement (Figure 3(e)) and a ~ 25
 276 m/s eastward wind enhancement (Figure 3(f)), whose phase fronts, when extrapolated
 277 down to lower latitudes, intersect the evening ST between $\sim -20^\circ$ to -25° latitude (~ 18.6
 278 SLT). The scale size of this feature is ~ 2500 km, comparable to the NH winter STW,
 279 and its phase front is inclined $\sim 41^\circ$ relative to the ST at the intersection point. Although
 280 there is also a strong northward wind component close to the evening ST and therefore
 281 associated with the evening STW during NH summer, a data artifact near the ST pre-
 282 vents us from characterizing it fully.

MIGHTI NH Winter Zonal Wind (~283 km): Migrating Tide Removal

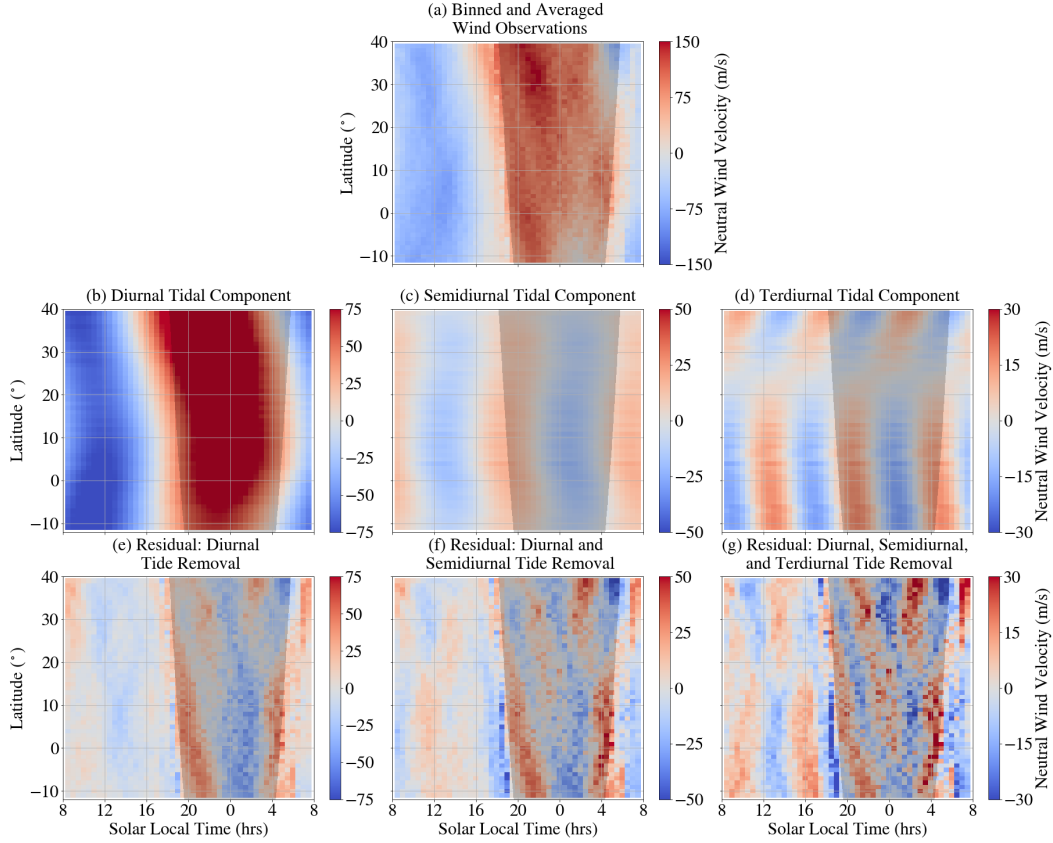


Figure 2. Same as Figure 1, but for the observed zonal wind component.

283 In combined equinox, the STW is less evident, even after removing diurnal tides
 284 (Figures 3(c) and 3(d)), consistent with Forbes et al. (2008)’s findings of seasonal asym-
 285 metry.

286 The NH winter and NH summer STWs mirror each other. The NH winter STW
 287 wavefront stretches from northwest to southeast with winds blowing northeast, while the
 288 NH summer STW wavefront extends from northeast to southwest with winds blowing
 289 southeast. Both have phase fronts inclined relative to the ST and intersect it $\sim 20^\circ$ off
 290 the equator in the winter hemisphere, near 18.7 SLT. The persistent presence of the STW
 291 in solstice winds, even with long-term averaging, shows that it is a robust feature. While
 292 there is likely day-to-day variability, the large average magnitude of the STW implies
 293 that it is a dominant feature in thermospheric winds, at least under solstice solar quiet
 294 conditions.

295 While it is tempting to quantitatively compare our estimated amplitudes to pre-
 296 vious studies, each study used a different filtering method, so it is necessary to use cau-
 297 tion. Miyoshi et al. (2009) removed diurnal, semidiurnal, and terdiurnal tidal compo-
 298 nents from their simulation results, Forbes et al. (2008) applied high-pass filtering with
 299 a 4800 km wavelength cutoff to CHAMP neutral density data, and H. Liu et al. (2009)
 300 subtracted a 3rd order polynomial from CHAMP densities and zonal winds along each
 301 satellite track. This makes an analogous ICON analysis impossible due to the difference
 302 in orbital inclinations. Both Vadas et al. (2023) and Chou et al. (2022) presented un-
 303 filtered simulation results. The figures we show are binned and averaged to remove the

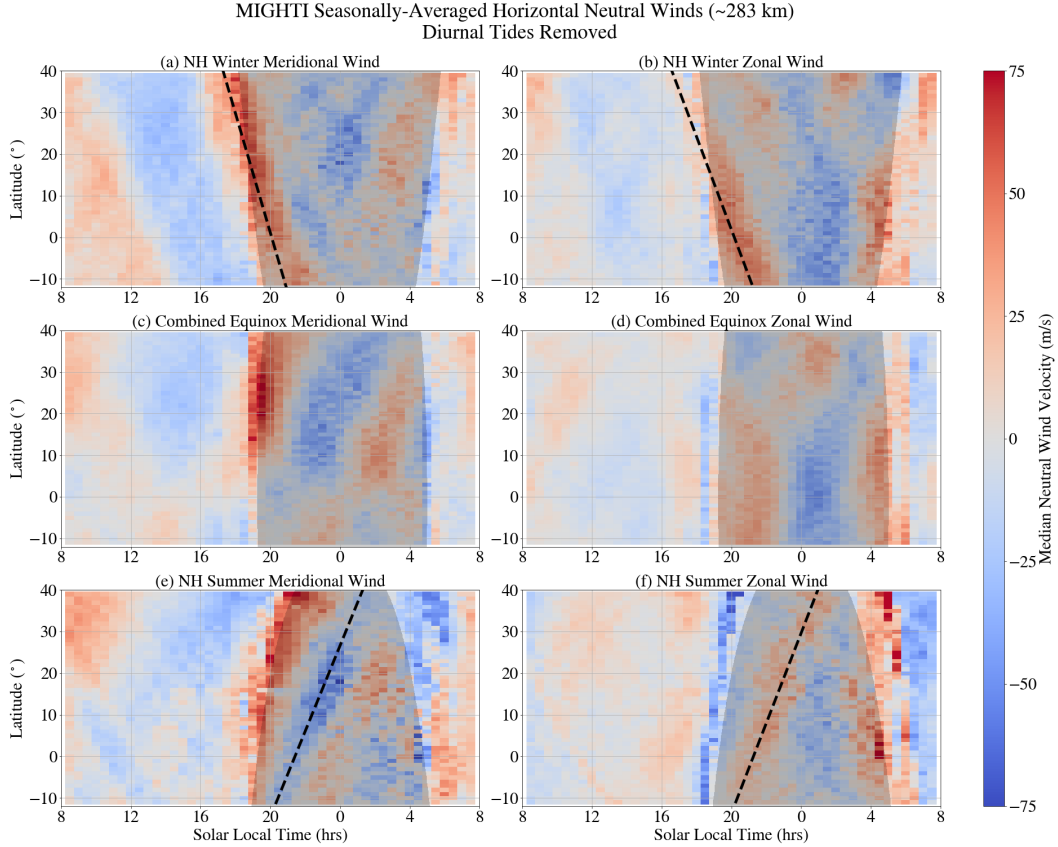


Figure 3. Binned and averaged MIGHTI meridional (left column) and zonal (right column) neutral winds for NH winter (top row), combined equinox (middle row), and NH summer (bottom row). Diurnal tides have been removed. Northward and eastward winds are positive. The gray shading shows the portion of the latitude/SLT space that is in darkness for each season. Clear STW features are marked by a black dotted line for the solstice cases ((a), (b), (e), and (f)).

304 non-migrating tidal features, and we report STW amplitudes after having removed the
305 diurnal tide.

306 Analyzing simulation outputs alongside MIGHTI observations provides insight into
307 the origins of STWs. Figure 4 displays NH winter meridional winds simulated by four
308 different models, all with diurnal tides removed. In the TIEGCM run without HMEs (Fig-
309 ure 4(a)), there is no clear STW signature, though a weak (~ 25 m/s) signature appears
310 when HMEs are included (Figure 4(b)). In contrast, both SD-WACCM-X (Figure 4(c))
311 and HIAMCM simulations (Figure 4(d)) exhibit a distinct STW signature. Both mod-
312 els overestimate the STW amplitude relative to observations, with SD-WACCM-X pro-
313 ducing ~ 60 m/s northward winds and HIAMCM producing ~ 100 m/s northward winds.
314 It is important to be cautious when interpreting the HIAMCM’s STW amplitude, how-
315 ever, as it is based on a single day and is not averaged like the other models and obser-
316 vations. The slight amplitude overestimation in SD-WACCM-X is real since the SD-WACCM-
317 X simulations are sampled identically to MIGHTI. Both models generally capture the
318 STW’s scale size and phase front inclination with respect to the ST.

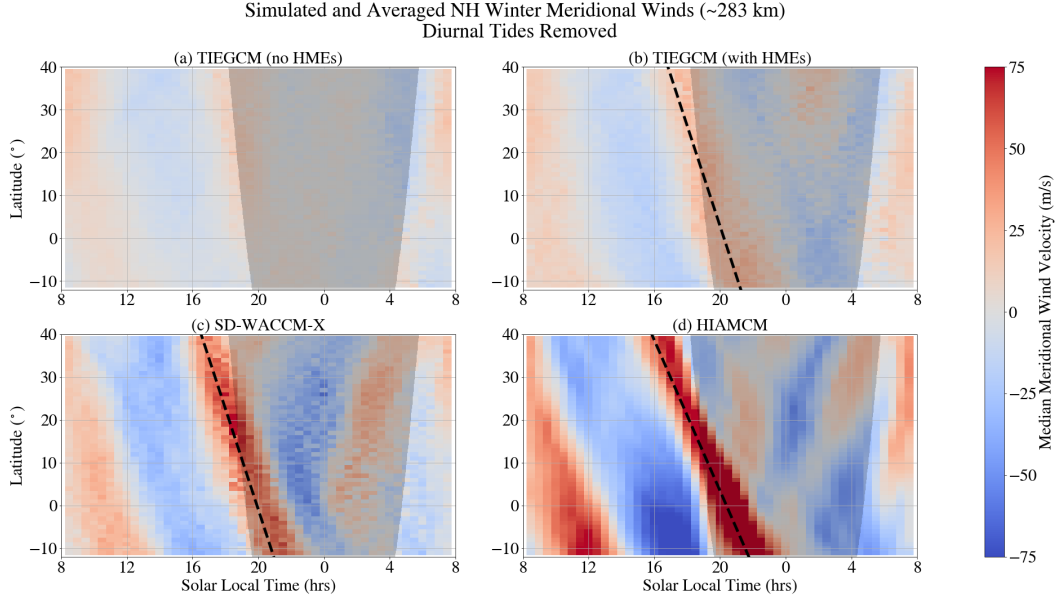


Figure 4. Each panel shows NH winter meridional winds binned by latitude and SLT with diurnal tides removed (the same as Figure 3(a)), but for (a) TIEGCM simulations without HME inputs, (b) TIEGCM simulations with HMEs derived from MIGHTI observations, (c) SD-WACCM-X simulations, and (d) HIAMCM simulations. The first three simulation results incorporate winter 2019 and 2020, while the HIAMCM result is from 15 January 15 2022.

319 The same figure, but showing the modeled zonal winds, is presented in Figure 5.
 320 Again, the TIEGCM run without HMEs (Figure 5(a)) shows little evidence of an evening
 321 STW. The case with HMEs does show an eastward wind enhancement near the evening
 322 ST, but the phase front is not comparably inclined with respect to the ST as the observed
 323 STW and does not intersect the ST at the sampled latitudes. Therefore, even with HMEs
 324 driving the lower boundary, the TIEGCM does not appear to accurately reproduce the
 325 observed evening STW. Both the SD-WACCM-X and HIAMCM simulations capture the
 326 STW signature in the zonal winds, although the signal does not diminish on the day-
 327 side as much as it does in the observations. Further discussion on the implications of STW
 328 appearance or absence in the various models is found in Section 4.

329 Figures 6(a) and 6(b) display the altitude structure of the NH winter STW in MIGHTI
 330 meridional winds and zonal winds, respectively. The data have been averaged data be-
 331 tween 10° and 20° latitude, where the STW intersects the ST, and diurnal tides have
 332 been removed. Although MIGHTI data is available between 109 and 200 km during the
 333 day, the nighttime gap precluded the removal of diurnal tides at these altitudes, so we
 334 do not report any data in this altitude range.

335 Above 200 km, where nighttime MIGHTI data is available, the STW either does
 336 not propagate vertically or has a vertical wavelength greater than 200 kilometers. Be-
 337 low 115 km, the STW is not distinguishable, although it may be masked by the large-
 338 amplitude tides at these altitudes. The SD-WACCM-X (Figure 6(c) and 6(d)) and HI-
 339 AMCM (Figure 6(e) and 6(f)) simulations similarly suggest a nearly constant phase
 340 with altitude above 200 km. In their simulations, Miyoshi et al. (2009) similarly reported a
 341 nearly constant phase line with altitude above 250 km, descending with local time be-
 342 low. Below 200 km, both simulations show a descent of the phase line with local time,
 343 possibly indicating upward wave propagation. The variation with altitude for the NH

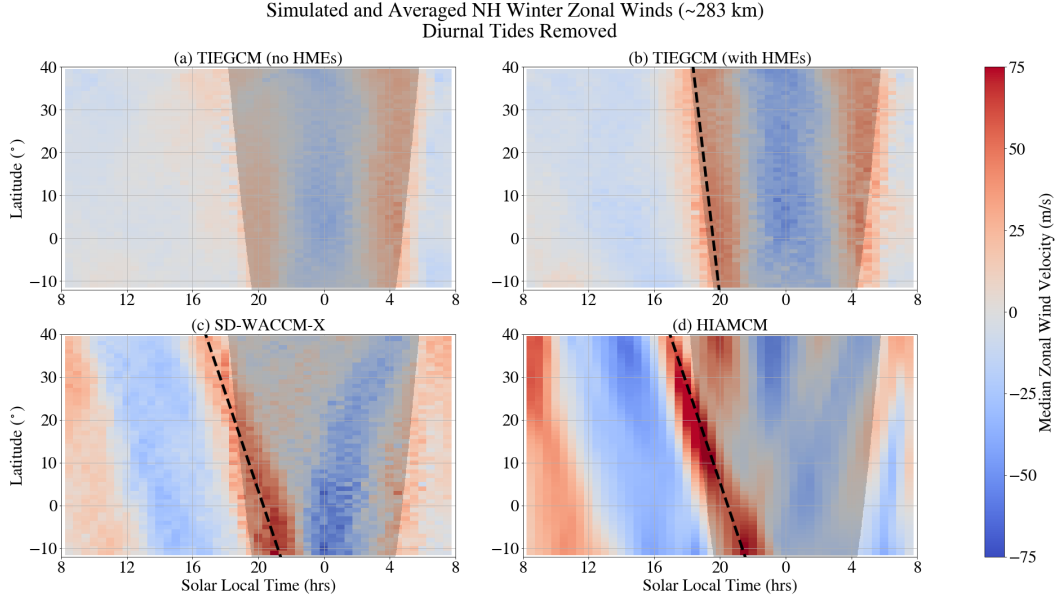


Figure 5. Same as Figure 4, but for the modeled zonal wind component.

344 summer case for MIGHTI observations and SD-WACCM-X simulations are presented
345 in Figure 7.

346 4 Discussion

347 While STWs are believed to arise from traveling atmospheric pressure and tem-
348 perature gradients, precisely where they originate in the atmosphere remains uncertain.
349 Bepalova et al. (2016) suggested that neutral density perturbations observed following
350 the ST might result from gravity waves generated in situ in the thermosphere by solar
351 extreme ultra violet (EUV) heating gradients. In contrast, Forbes et al. (2008) suggested
352 that STWs may propagate up from the lower atmosphere, possibly initiated by UV heat-
353 ing of mesospheric ozone, as initially proposed by Chimonas and Hines (1970).

354 Our analysis reveals a significant STW signature in solstice neutral wind observa-
355 tions. Both SD-WACCM-X and HIAMCM simulations capture the STW scale size and
356 inclination relative to the ST, although the simulated STWs exceed the observed STW
357 amplitudes. In contrast, TIEGCM simulations lack the STW signature, although intro-
358 ducing HMEs at the lower boundary leads to the emergence of a weak (~ 25 m/s) sig-
359 nature in the meridional wind component.

360 Both SD-WACCM-X and HIAMCM simulate the atmosphere down to Earth’s sur-
361 face (H.-L. Liu et al., 2018; Becker & Vadas, 2020), whereas the TIEGCM cannot self-
362 consistently resolve atmospheric processes below its 97 km lower boundary (Qian et al.,
363 2014). Including ICON HMEs into the TIEGCM partially accounts for lower atmospheric
364 effects by including data-informed diurnal and semidiurnal tidal propagation up from
365 the lower atmosphere (Maute et al., 2023). The presence of STW signatures in models
366 with the lower atmosphere but their absence in those without suggests that the lower
367 atmosphere plays an important role in STW generation. This aligns with Miyoshi et al.
368 (2009), who found that excluding atmospheric dynamics below 80 km in their simula-
369 tions resulted in the disappearance of STW signatures. Further, the weak STW signa-
370 ture in the TIEGCM simulations with ICON HMEs implies that diurnal and semidiur-

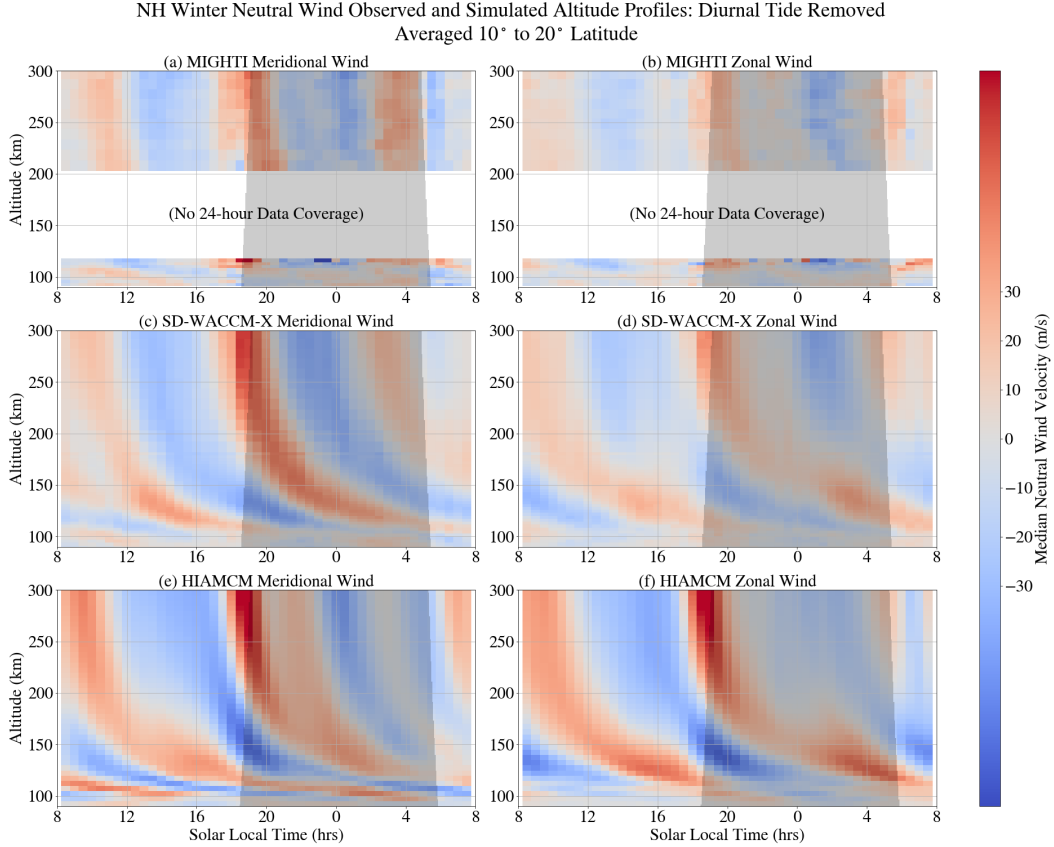


Figure 6. NH winter meridional (left) and zonal (right) winds averaged between 10° and 20° latitude as a function of altitude and SLT for (top) MIGHTI data (winter 2019 and 2020), (middle) SD-WACCM-X simulations (winter 2019 and 2020), and (bottom) HIAMCM simulations (15 January 2022). Diurnal tides have been removed. The gray shading shows the portion of the altitude/SLT space that is in darkness. Northward and eastward winds are defined to be positive.

371 nal tides from the lower and middle atmosphere contribute to, but cannot fully explain,
 372 the STW. Although Miyoshi et al. (2009) found that upward propagating migrating tides
 373 contributed to STW formation, they suggested that STWs mainly arise from a super-
 374 position of these tides with zonal wavenumbers 4 to 6, while our results suggest that lower-
 375 order tides also play an important role.

376 Differences in how the models account for gravity wave effects may also affect their
 377 ability to reproduce STWs. STWs could be large-scale gravity waves which either propa-
 378 gate directly from the lower/middle atmosphere to the thermosphere, or which are indi-
 379 rectly generated in the thermosphere through the dissipation of upward-propagating
 380 gravity waves (Vadas, 2007; Lund & Fritts, 2012; Heale et al., 2014). This latter ‘indi-
 381 rect’ mechanism would arise because gravity wave dissipation by molecular viscosity de-
 382 pends critically on the background temperature, resulting in larger amplitude force/heating
 383 at lower altitudes on the nightside of the ST (Vadas, 2007). The resulting ‘jump’ in the
 384 force/heating across the ST from gravity wave dissipation could then generate large-scale
 385 secondary gravity waves (Vadas, 2013).

386 Large-scale gravity waves arising from the ST passage would be captured by SD-
 387 WACCM-X and the HIAMCM, which resolve gravity waves from below, but not by the

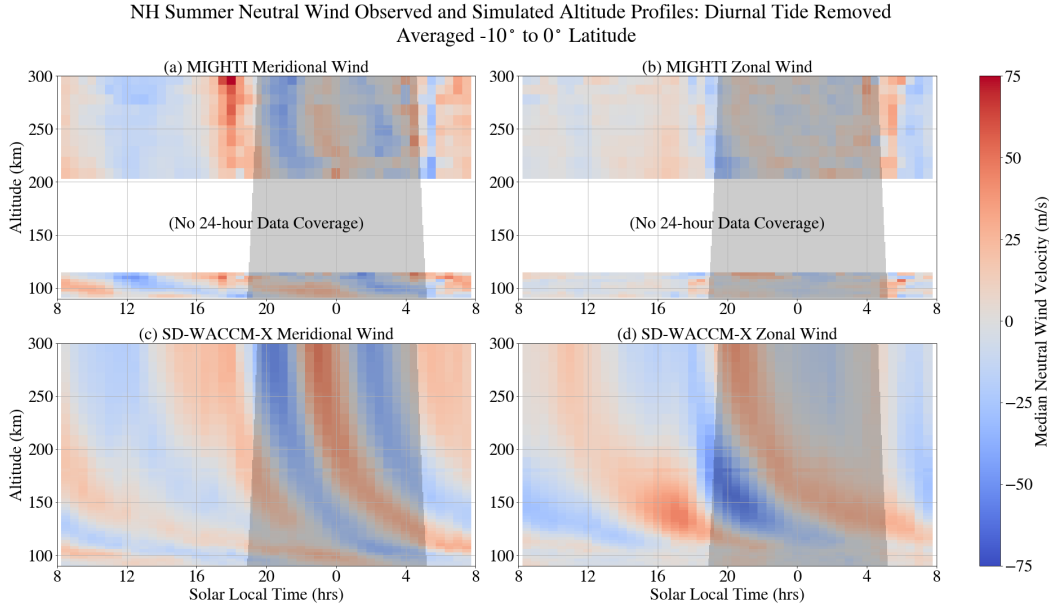


Figure 7. NH summer meridional (left) and zonal (right) winds averaged between -10° and 0° latitude as a function of altitude and SLT for (top) MIGHTI data (winter 2019 and 2020), (bottom) SD-WACCM-X simulations (winter 2019 and 2020). Diurnal tides have been removed. The gray shading shows the portion of the altitude/SLT space that is in darkness. Northward and eastward winds are defined to be positive.

388 TIEGCM. Although direct EUV heating can also generate gravity waves (Chimonas &
 389 Hines, 1970; Vadas, 2013), the absence of STWs in the TIEGCM simulations suggests
 390 this mechanism is less significant. Notably, the amplitudes of stratospheric gravity waves
 391 have been found to be larger during solstice than equinox (Figure 6 of Hoffmann et al.,
 392 2013; Cullens et al., 2022), consistent with our finding of larger STW amplitudes dur-
 393 ing solstices, further supporting their potential connection to gravity waves.

394 Future modeling studies will investigate these mechanisms, as well as possible non-
 395 linear tidal interactions, as the source of the STWs. Furthermore, the reason for the evening
 396 STW’s inclination with respect to the ST remains an open question which future mod-
 397 eling should address.

398 Although we reported significant evening STWs, we do not observe any compara-
 399 ble signature near the morning ST. Both Forbes et al. (2008) and H. Liu et al. (2009)
 400 also noted this asymmetry, finding morning STWs to be less well-defined than their evening
 401 counterparts. H. Liu et al. (2009) postulated that larger neutral temperature gradients
 402 near the evening ST, as suggested by modeled neutral temperatures at 400 km, may make
 403 wave generation more efficient in the evening. Some authors suggested the opposite, claim-
 404 ing that the morning heating process is more efficient than evening cooling, resulting in
 405 a sharper sunrise gradient which produces smaller scale STWs (Somsikov & Ganguly,
 406 1995).

407 Indeed, both Chou et al. (2022) and Vadas et al. (2023) report a smaller scale, weaker
 408 amplitude morning STW in their simulation results. Ionospheric studies have also shown
 409 evidence of morning STWs (Galushko et al., 1998; Afraimovich, 2008; Song et al., 2013;
 410 Ding et al., 2014). For example, Zhang et al. (2021) measured post-sunrise electron den-
 411 sity perturbations using the Millstone Hill Incoherent Scatter Radar (ISR), identifying

412 traveling ionospheric disturbances (TIDs) with zonal wavelengths of ~ 445 km. If similarly-
 413 sized thermospheric disturbances accompany these TIDs, it is unlikely that MIGHTI would
 414 be able to resolve them due to its horizontal resolution.

415 The thermospheric evening STW may play a currently under-recognized role in driv-
 416 ing ionospheric dynamics. The large-amplitude winds reported in this study could in-
 417 fluence ionospheric circulation through ion drag or dynamo effects. The meridional STW
 418 winds can push plasma along magnetic field lines, contributing to the summer to win-
 419 ter hemisphere redistribution of plasma (Heelis et al., 2022) and affecting the plasma den-
 420 sity altitude distribution. Additionally, the zonal STW winds, when blowing across the
 421 westward conductivity gradient caused by changing solar input, may influence the up-
 422 ward plasma drifts of the prereversal enhancement (PRE) (Richmond et al., 2015; H.-
 423 L. Liu, 2020). Variability in STWs may thus affect the PRE, which, in turn, is closely
 424 linked to equatorial plasma bubble (EPB) variability (Fejer et al., 1999).

425 5 Conclusion

426 Leveraging ~ 1.5 years of MIGHTI data, this study reported the first remotely-sensed
 427 observations of evening STWs, revealing them as one of the most prominent recurring
 428 features in the neutral winds above 200 km during solstices. The STW meridional wind
 429 component, reported for the first time, has a similar (and sometimes larger) magnitude
 430 compared to the zonal component, indicating that STW winds blow predominantly north-
 431 eastward during NH winter and southeastward during NH summer. Furthermore, we pro-
 432 vided the first observational altitude profile of a STW, revealing vertical wavelengths longer
 433 than several hundred kilometers above 200 km. Model comparisons suggested that STW
 434 generation is strongly influenced by the lower atmosphere and may result from large-scale
 435 gravity waves or their interactions with atmospheric tides.

436 Given their substantial and persistent presence, STWs hold intrinsic scientific sig-
 437 nificance, potentially serving as key drivers of thermospheric and ionospheric processes.
 438 Future research endeavors, including modeling and observations, are crucial for unrav-
 439 eling the origins and daily variability of these waves, fostering a deeper understanding
 440 of their impact on Earth’s upper atmosphere.

441 Acknowledgments

442 ICON is supported by NASA’s Explorers Program through contracts NNG12FA45C and
 443 NNG12FA42I. SLV and EB were supported by NSF grant # AGS-1832988 and NASA
 444 grant # 80NSSC22K0174. AM is supported by NASA award # 80NSSC23K1123

445 Open Research

446 This analysis used ICON/MIGHTI neutral wind data, Level 2.2, Version 5, which is avail-
 447 able from <https://icon.ssl.berkeley.edu/Data> and <https://cdaweb.gsfc.nasa.gov/pub/data/icon/>. The WACCM-X simulations used in this work are available from <https://doi.org/10.5065/rjgt-g951>. The TIEGCM-ICON simulations Level 4 V01 are avail-
 448 able at <https://cdaweb.gsfc.nasa.gov/pub/data/icon/14/>. The HIAMCM simu-
 449 lation is available at [https://www.cora.nwra.com/vadas/Vadas-etal-JGR-2023-TongaICON-
 450 files/](https://www.cora.nwra.com/vadas/Vadas-etal-JGR-2023-TongaICON-files/)
 451
 452

453 References

- 454 Afraimovich, E. (2008). First GPS-TEC evidence for the wave structure excited by
 455 the solar terminator. *Earth, planets and space*, *60*, 895–900.
 456 Becker, E., Goncharenko, L., Harvey, V. L., & Vadas, S. L. (2022). Multi-step ver-
 457 tical coupling during the January 2017 sudden stratospheric warming. *Journal*

- 458 of *Geophysical Research: Space Physics*, 127(12), e2022JA030866.
- 459 Becker, E., & Vadas, S. L. (2020). Explicit global simulation of gravity waves in
460 the thermosphere. *Journal of Geophysical Research: Space Physics*, 125(10),
461 e2020JA028034.
- 462 Becker, E., Vadas, S. L., Bossert, K., Harvey, V. L., Zülicke, C., & Hoffmann, L.
463 (2022). A high-resolution whole-atmosphere model with resolved gravity waves
464 and specified large-scale dynamics in the troposphere and stratosphere. *Jour-
465 nal of Geophysical Research: Atmospheres*, 127(2), e2021JD035018.
- 466 Beer, T. (1973). Supersonic generation of atmospheric waves. *Nature*, 242(5392),
467 34–34.
- 468 Beer, T. (1978). On atmospheric wave generation by the terminator. *Planetary and
469 Space Science*, 26(2), 185–188.
- 470 Bespalova, A., Fedorenko, A., Cheremnykh, O., & Zhuk, I. (2016). Satellite observa-
471 tions of wave disturbances caused by moving solar terminator. *Journal of At-
472 mospheric and Solar-Terrestrial Physics*, 140, 79–85.
- 473 Chimonas, G., & Hines, C. O. (1970). Atmospheric gravity waves induced by a solar
474 eclipse. , 75(4), 875–875. doi: 10.1029/JA075i004p00875
- 475 Chou, M.-Y., Yue, J., Sassi, F., McDonald, S., Tate, J., Pedatella, N., . . . Harvey,
476 V. L. (2022). Modeling the day-to-day variability of midnight equatorial
477 plasma bubbles with SAMI3/SD-WACCM-X. *Journal of Geophysical Research:
478 Space Physics*, e2023JA031585.
- 479 Colonna, R., & Tramutoli, V. (2021). A new model of solar illumination of earth’s
480 atmosphere during night-time. *Earth*, 2(2), 191–207.
- 481 Cot, C., & Teitelbaum, H. (1980). Generation of gravity waves by inhomogeneous
482 heating of the atmosphere. *Journal of Atmospheric and Terrestrial Physics*,
483 42(9-10), 877–883.
- 484 Cullens, C. Y., England, S. L., Immel, T. J., Maute, A., Harding, B. J., Triplett,
485 C. C., . . . Stevens, M. H. (2022). Seasonal variations of medium-scale
486 waves observed by ICON-MIGHTI. *Geophysical Research Letters*, 49(17),
487 e2022GL099383.
- 488 Cullens, C. Y., Immel, T. J., Triplett, C. C., Wu, Y.-J., England, S. L., Forbes,
489 J. M., & Liu, G. (2020). Sensitivity study for ICON tidal analysis. *Progress in
490 Earth and Planetary Science*, 7, 1–13.
- 491 Ding, F., Wan, W., Li, Q., Zhang, R., Song, Q., Ning, B., . . . Xiong, B. (2014).
492 Comparative climatological study of large-scale traveling ionospheric distur-
493 bances over north america and china in 2011–2012. *Journal of Geophysical
494 Research: Space Physics*, 119(1), 519–529.
- 495 Drob, D., Emmert, J., Crowley, G., Picone, J., Shepherd, G., Skinner, W., . . . others
496 (2008). An empirical model of the Earth’s horizontal wind fields: HWM07.
497 *Journal of Geophysical Research: Space Physics*, 113(A12).
- 498 England, S. L., Englert, C. R., Harding, B. J., Triplett, C. C., Marr, K., Harlander,
499 J. M., . . . Immel, T. J. (2022). Vertical shears of horizontal winds in the
500 lower thermosphere observed by ICON. *Geophysical Research Letters*, 49(11),
501 e2022GL098337.
- 502 Englert, C. R., Harlander, J. M., Brown, C. M., Marr, K. D., Miller, I. J., Stump,
503 J. E., . . . others (2017). Michelson interferometer for global high-resolution
504 thermospheric imaging (MIGHTI): instrument design and calibration. *Space
505 science reviews*, 212, 553–584.
- 506 Englert, C. R., Harlander, J. M., Marr, K. D., Harding, B. J., Makela, J. J., Fae, T.,
507 . . . Immel, T. J. (2023). Michelson Interferometer for Global High-resolution
508 Thermospheric Imaging (MIGHTI) on-orbit wind observations: Data analysis
509 and instrument performance. *Space Science Reviews*, 219(3), 27.
- 510 Fejer, B. G., Scherliess, L., & De Paula, E. (1999). Effects of the vertical plasma
511 drift velocity on the generation and evolution of equatorial spread F. *Journal
512 of Geophysical Research: Space Physics*, 104(A9), 19859–19869.

- 513 Forbes, J., Bruinsma, S. L., Miyoshi, Y., & Fujiwara, H. (2008). A solar terminator
514 wave in thermosphere neutral densities measured by the CHAMP satellite.
515 *Geophysical Research Letters*, *35*(14).
- 516 Forbes, J., Zhang, X., Hagan, M. E., England, S. L., Liu, G., & Gasperini, F. (2017).
517 On the specification of upward-propagating tides for ICON science investiga-
518 tions. *Space Science Reviews*, *212*, 697–713.
- 519 Galushko, V., Paznukhov, V., Yampolski, Y., & Foster, J. (1998). Incoherent scatter
520 radar observations of AGW/TID events generated by the moving solar
521 terminator. In *Annales geophysicae* (Vol. 16, pp. 821–827).
- 522 Garcia, R. R., Smith, A. K., Kinnison, D. E., de la Cámara, Á., & Murphy, D. J.
523 (2017). Modification of the gravity wave parameterization in the Whole At-
524 mosphere Community Climate Model: Motivation and results. *Journal of the*
525 *Atmospheric Sciences*, *74*(1), 275–291.
- 526 Harding, B. J., Chau, J. L., He, M., Englert, C. R., Harlander, J. M., Marr, K. D.,
527 ... others (2021). Validation of ICON-MIGHTI thermospheric wind ob-
528 servations: 2. Green-line comparisons to specular meteor radars. *Journal of*
529 *Geophysical Research: Space Physics*, *126*(3), e2020JA028947.
- 530 Harding, B. J., Makela, J. J., Englert, C. R., Marr, K. D., Harlander, J. M., Eng-
531 land, S. L., & Immel, T. J. (2017). The MIGHTI wind retrieval algorithm:
532 Description and verification. *Space Science Reviews*, *212*, 585–600.
- 533 Harlander, J. M., Englert, C. R., Brown, C. M., Marr, K. D., Miller, I. J., Zastera,
534 V., ... Mende, S. B. (2017). Michelson interferometer for global high-
535 resolution thermospheric imaging (MIGHTI): monolithic interferometer design
536 and test. *Space science reviews*, *212*, 601–613.
- 537 Heale, C., Snively, J., Hickey, M., & Ali, C. (2014). Thermospheric dissipation of
538 upward propagating gravity wave packets. *Journal of Geophysical Research:*
539 *Space Physics*, *119*(5), 3857–3872.
- 540 Heelis, R. A., Chen, Y.-J., Depew, M., Harding, B. J., Immel, T. J., Wu, Y.-J., ...
541 others (2022). Topside plasma flows in the equatorial ionosphere and their
542 relationships to F-region winds near 250 km. *Journal of Geophysical Research:*
543 *Space Physics*, *127*(5), e2022JA030415.
- 544 Hoffmann, L., Xue, X., & Alexander, M. (2013). A global view of stratospheric grav-
545 ity wave hotspots located with Atmospheric Infrared Sounder observations.
546 *Journal of Geophysical Research: Atmospheres*, *118*(2), 416–434.
- 547 Immel, T. J., England, S., Mende, S., Heelis, R., Englert, C., Edelstein, J., ... oth-
548 ers (2018). The Ionospheric Connection Explorer mission: Mission goals and
549 design. *Space Science Reviews*, *214*, 1–36.
- 550 Immel, T. J., England, S. L., Harding, B. J., Wu, Y.-J., Maute, A., Cullens, C., ...
551 others (2023). The Ionospheric Connection Explorer-Prime mission review.
552 *Space Science Reviews*, *219*(5), 41.
- 553 Lindzen, R. S. (1981). Turbulence and stress owing to gravity wave and tidal break-
554 down. *Journal of Geophysical Research*, *68*(C10), 9707–9714.
- 555 Liu, H., Lühr, H., & Watanabe, S. (2009). A solar terminator wave in thermospheric
556 wind and density simultaneously observed by CHAMP. *Geophysical Research*
557 *Letters*, *36*(10).
- 558 Liu, H.-L. (2020). Day-to-day variability of prereversal enhancement in the verti-
559 cal ion drift in response to large-scale forcing from the lower atmosphere. *Space*
560 *Weather*, *18*(4), e2019SW002334.
- 561 Liu, H.-L., Bardeen, C. G., Foster, B. T., Lauritzen, P., Liu, J., Lu, G., ... others
562 (2018). Development and validation of the Whole Atmosphere Community
563 Climate Model with thermosphere and ionosphere extension (WACCM-X 2.0).
564 *Journal of Advances in Modeling Earth Systems*, *10*(2), 381–402.
- 565 Lund, T. S., & Fritts, D. C. (2012). Numerical simulation of gravity wave break-
566 ing in the lower thermosphere. *Journal of Geophysical Research: Atmospheres*,
567 *117*(D21).

- 568 Marsh, D. R., Mills, M. J., Kinnison, D. E., Lamarque, J.-F., Calvo, N., & Polvani,
569 L. M. (2013). Climate change from 1850 to 2005 simulated in CESM1
570 (WACCM). *Journal of climate*, *26*(19), 7372–7391.
- 571 Maute, A. (2017). Thermosphere-ionosphere-electrodynamics general circulation
572 model for the ionospheric connection explorer: TIEGCM-ICON. *Space Science*
573 *Reviews*, *212*(1-2), 523–551.
- 574 Maute, A., Forbes, J. M., Cullens, C. Y., & Immel, T. J. (2023). Delineating the
575 effect of upward propagating migrating solar tides with the TIEGCM-ICON.
576 *Frontiers in Astronomy and Space Sciences*, *10*, 1147571.
- 577 McGinness, E. C., Immel, T. J., Harding, B. J., Wu, Y.-J., & Triplett, C. C. (2023).
578 The effects of a small geomagnetic storm on earth’s thermosphere and iono-
579 sphere: ICON observations of the 25 January 2021 disturbance. *Journal of*
580 *Geophysical Research: Space Physics*, *128*(7), e2022JA031207.
- 581 Miyoshi, Y., Fujiwara, H., Forbes, J. M., & Bruinsma, S. L. (2009). Solar terminator
582 wave and its relation to the atmospheric tide. *Journal of Geophysical Research:*
583 *Space Physics*, *114*(A7).
- 584 Neale, R. B., Richter, J., Park, S., Lauritzen, P. H., Vavrus, S. J., Rasch, P. J., &
585 Zhang, M. (2013). The mean climate of the Community Atmosphere Model
586 (CAM4) in forced SST and fully coupled experiments. *Journal of Climate*,
587 *26*(14), 5150–5168.
- 588 Picone, J., Hedin, A., Drob, D. P., & Aikin, A. (2002). NRLMSISE-00 empirical
589 model of the atmosphere: Statistical comparisons and scientific issues. *Journal*
590 *of Geophysical Research: Space Physics*, *107*(A12), SIA–15.
- 591 Qian, L., Burns, A. G., Emery, B. A., Foster, B., Lu, G., Maute, A., ... Wang, W.
592 (2014). The NCAR TIE-GCM: A community model of the coupled thermo-
593 sphere/ionosphere system. *Modeling the ionosphere-thermosphere system*,
594 73–83.
- 595 Richmond, A. (1995). Ionospheric electrodynamics using magnetic apex coordinates.
596 *Journal of geomagnetism and geoelectricity*, *47*(2), 191–212.
- 597 Richmond, A., Fang, T.-W., & Maute, A. (2015). Electrodynamics of the equato-
598 rial evening ionosphere: 1. Importance of winds in different regions. *Journal of*
599 *Geophysical Research: Space Physics*, *120*(3), 2118–2132.
- 600 Richter, J. H., Sassi, F., & Garcia, R. R. (2010). Toward a physically based gravity
601 wave source parameterization in a general circulation model. *Journal of the At-*
602 *mospheric Sciences*, *67*(1), 136–156.
- 603 Somsikov, V. (1987). A spherical model of wave generation in the atmosphere by the
604 solar terminator. *Journal of atmospheric and terrestrial physics*, *49*(5), 433–
605 438.
- 606 Somsikov, V. (2011). Solar terminator and dynamic phenomena in the atmosphere:
607 A review. *Geomagnetism and Aeronomy*, *51*, 707–719.
- 608 Somsikov, V., & Ganguly, B. (1995). On the formation of atmospheric inhomog-
609 eneities in the solar terminator region. *Journal of Atmospheric and Terres-*
610 *trial Physics*, *57*(12), 1513–1523.
- 611 Song, Q., Ding, F., Wan, W., Ning, B., Liu, L., Zhao, B., ... Zhang, R. (2013). Sta-
612 tistical study of large-scale traveling ionospheric disturbances generated by the
613 solar terminator over China. *Journal of Geophysical Research: Space Physics*,
614 *118*(7), 4583–4593.
- 615 Vadas, S. L. (2007). Horizontal and vertical propagation and dissipation of gravity
616 waves in the thermosphere from lower atmospheric and thermospheric sources.
617 *Journal of Geophysical Research: Space Physics*, *112*(A6).
- 618 Vadas, S. L. (2013). Compressible f-plane solutions to body forces, heatings, and
619 coolings, and application to the primary and secondary gravity waves gener-
620 ated by a deep convective plume. *Journal of Geophysical Research: Space*
621 *Physics*, *118*(5), 2377–2397.
- 622 Vadas, S. L., Becker, E., Figueiredo, C., Bossert, K., Harding, B. J., & Gasque, L. C.

- 623 (2023). Primary and secondary gravity waves and large-scale wind changes
624 generated by the Tonga volcanic eruption on 15 January 2022: Modeling and
625 comparison with ICON-MIGHTI winds. *Journal of Geophysical Research:*
626 *Space Physics*, *128*(2), e2022JA031138.
- 627 Wu, Y.-J. J., Harding, B. J., Triplett, C. C., Makela, J. J., Marr, K. D., Englert,
628 C. R., ... Immel, T. J. (2020). Errors from asymmetric emission rate
629 in spaceborne, limb sounding Doppler interferometry: A correction algo-
630 rithm with application to ICON/MIGHTI. *Earth and Space Science*, *7*(10),
631 e2020EA001164.
- 632 Wu, Y.-J. J., Mende, S., Harding, B. J., Alken, P., Maute, A., & Immel, T. J.
633 (2023). Cross-validation of the ionospheric vertical drift measurements based
634 on ICON/IVM, Swarm, and the Ground-Based Radar at the Jicamarca Radio
635 Observatory. *Space Science Reviews*, *219*(6), 47.
- 636 Zhang, S.-R., Erickson, P. J., Gasque, L., Aa, E., Rideout, W., Vierinen, J., ...
637 Coster, A. J. (2021). Electrified postsunrise ionospheric perturbations at
638 Millstone Hill. *Geophysical Research Letters*, *48*(18), e2021GL095151.